

FarSLIP: Discovering Effective CLIP Adaptation for Fine-Grained Remote Sensing Understanding

Zhenshi Li^{1,2} Weikang Yu³ Dilxat Muhtar¹ Xueliang Zhang^{1,*} Pengfeng Xiao¹,
Pedram Ghamisi³ Xiao Xiang Zhu^{2,*}

¹Nanjing University ²Technical University of Munich ³Helmholtz-Zentrum Dresden-Rossendorf
Lzhenshi@outlook.com, zxl@nju.edu.cn, xiaoxiang.zhu@tum.de

Abstract

As CLIP’s global alignment limits its ability to capture fine-grained details, recent efforts have focused on enhancing its region-text alignment. However, current remote sensing (RS)-specific CLIP variants still inherit this limited spatial awareness. We identify two key limitations behind this: (1) current RS image-text datasets generate global captions from object-level labels, leaving the original object-level supervision underutilized; (2) despite the success of region-text alignment methods in general domain, their direct application to RS data often leads to performance degradation. To address these, we construct the first multi-granularity RS image-text dataset, MGRS-200k, featuring rich object-level textual supervision for RS region-category alignment. We further investigate existing fine-grained CLIP tuning strategies and find that current explicit region-text alignment methods, whether in a direct or indirect way, underperform due to severe degradation of CLIP’s semantic coherence. Building on these, we propose FarSLIP, a Fine-grained Aligned RS Language-Image Pretraining framework. Rather than the commonly used patch-to-CLS self-distillation, FarSLIP employs patch-to-patch distillation to align local and global visual cues, which improves feature discriminability while preserving semantic coherence. Additionally, to effectively utilize region-text supervision, it employs simple CLS token-based region-category alignment rather than explicit patch-level alignment, further enhancing spatial awareness. FarSLIP features improved fine-grained vision-language alignment in RS domain and sets a new state of the art not only on RS open-vocabulary semantic segmentation, but also on image-level tasks such as zero-shot classification and image-text retrieval. Our dataset, code, and models are available at <https://github.com/NJU-LHRS/FarSLIP>.

1. Introduction

Vision-language foundational models (VLFMs), such as CLIP [45], have exhibited remarkable generalizability across diverse downstream tasks. Thanks to the rich set of real-world concepts encoded in VLFMs, they can be effectively transferred to other domains, achieving significantly higher accuracy than training from scratch [23, 39]. In the remote sensing (RS) community, promising in-domain performance is obtained by building RS-specific image-caption datasets and fully fine-tuning CLIP [31, 52], a strategy shown to be effective for CLIP’s domain adaptation [14].

Recent studies have shown that CLIP inherently exhibit superior localization capabilities, enabling training-free open-vocabulary semantic segmentation (OVSS) [25, 26, 50, 73]. This intrinsic capability also holds great potential for supporting domain-specific dense prediction tasks, such as land cover mapping in RS imagery [29] with more flexible and adaptable category systems. However, since CLIP is trained by aligning global image and text features, it still exhibits limited capability in achieving high-precision spatial recognition [2, 54, 55]. Therefore, recent studies have further aimed to enhance its inherent fine-grained associations by explicitly aligning region-level features with language. Approaches such as weakly supervised alignment [3, 40], large-scale object-text dataset construction [5, 72], and self-distillation [54, 64] have been proposed to further improve the performance on fine-grained tasks.

However, despite being specifically optimized for fine-grained recognition, these general-domain models still perform poorly on OVSS in RS images, even worse than the RS variants trained with simple vision-language contrastive learning (CL), as shown in Tab. 10, highlighting the importance of RS-specific fine-tuning. Furthermore, we find that these strategies are suboptimal when directly applied to RS domain. As shown in Fig. 1, directly applying state-of-the-art (SOTA) fine-grained CLIP adaptation methods to RS datasets even fails to surpass the original CLIP baseline.

*Corresponding author.

To better equip VLFMs for fine-grained RS interpretation, we consider current limitations from two aspects: data and methodology. On the data side, due to the inaccessibility of large-scale web-crawled image-text data for RS, existing RS datasets are typically constructed by generating global-level captions based on object-level information, sourced from object detection or segmentation datasets [31, 61], or from crowd-sourced geospatial database [38, 52]. We argue this paradigm underutilizes the rich regional cues in the original data as a source of fine-grained supervision. Hence, to advance fine-grained CLIP tuning in RS, we propose MGRS-200k, the first multi-granularity RS image-text dataset. Beyond global captions, as commonly seen in prior works, MGRS-200k features over 1M object-category annotations, supporting explicit region-level vision-language alignment for RS-domain CLIP tuning.

On the methodology side, motivated by the side effects of existing fine-grained CLIP tuning methods on RS (Fig. 1), we conduct a comprehensive analysis to understand their underlying causes. We find that current explicit region-text alignment approaches, whether direct patch-to-text alignment [20, 60] or indirect alignment via patch-to-CLS self-distillation [20, 54, 64], are in fact detrimental to CLIP tuning, as they substantially disrupt the model’s semantic coherence, a property shown to be crucial for fine-grained understanding [26, 42, 44, 55]. In order to overcome this, we identified that: (1) For direct region-category alignment via CL, tuning CLIP by aligning text with the CLS token rather than patch features [20, 60] not only improves feature discriminability and region-text alignment but also enhances semantic coherence; (2) For indirect region-text alignment via local-global self-distillation, we propose patch-to-patch distillation instead of the commonly used patch-to-CLS distillation [20, 54, 64], preserving semantic coherence while enhancing feature discriminability.

Following the above insights, we develop an RS-specific VLFM called FarSLIP. By employing the above-mentioned appropriate tuning strategies with the proposed multi-granularity RS image-text dataset, we enhance the CLIP’s understanding capabilities at both global and local levels for RS tasks. FarSLIP achieves SOTA performance across both fine-grained tasks (*e.g.*, OVSS) and global-level tasks such as zero-shot classification (ZSC) and cross-modal retrieval.

In summary, our contributions are threefold:

- We construct MGRS-200k, the first multi-granularity image-text dataset for RS, establishing a foundation for fine-grained RS-specific VLFM training.
- We conduct a thorough analysis of fine-grained CLIP tuning for RS, offering transferable insights for domain-specific fine-grained adaptation of CLIP.
- We propose FarSLIP, an RS-specialized VLFM that achieves SOTA performance on both global- and local-level RS multimodal tasks.

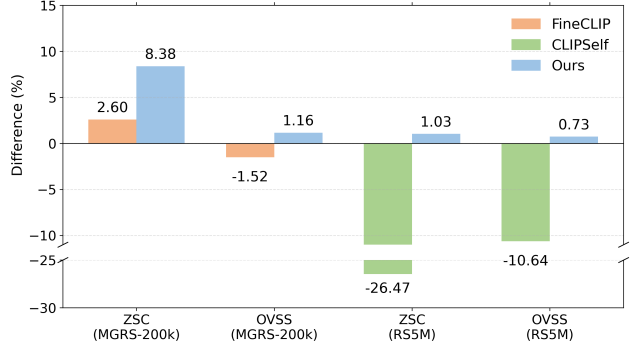


Figure 1. Accuracy differences relative to CLIP for models fine-tuned with SOTA methods, *e.g.*, FineCLIP [20] and CLIPSelf [54], on various RS datasets (shown in brackets). These models show only marginal improvement or even performance drops in most cases, indicating limited effectiveness for RS-domain application.

2. Related Work

2.1. Fine-grained Vision-Language Alignment

To enhance VLFMs’ fine-grained vision-language alignment, recent studies have explored self-supervised [22, 37, 41, 48] or weakly supervised objectives [1, 3, 40]. Given the high cost of training from scratch, most existing works focus on leveraging the pretrained capabilities of CLIP. One line of work explores self-distillation to exploit the frozen CLIP model’s own knowledge [20, 44, 54, 64], while another constructs large-scale region-text datasets to improve local-level alignment in feature space [5, 20, 60, 72]. However, these models lag behind RS CLIP variants without fine-grained training (Tab. 10), and even when trained on RS data, these methods achieve only limited improvements or introduce side effects (Fig. 1). How to effectively adapt CLIP for fine-grained RS interpretation remains unresolved.

2.2. Vision-Language Foundation Models for RS

Recent studies have built RS image-caption datasets to adapt CLIP with domain-specific knowledge, producing RS-specialized VLFMs [31, 52, 70]. However, their focus on global-level CL inherits CLIP’s limitations in fine-grained visual understanding. Moreover, due to the unavailability of large-scale RS image-text data on the web, current RS datasets commonly synthesize global captions by inputting region-level annotations, sourced from object detection, semantic segmentation datasets [31, 61] or geospatial information like OpenStreetMap [30, 38, 52], into large language models (LLMs) or multimodal LLMs. We argue that these approaches significantly underutilize the rich spatial and semantic object-level annotations already available in their source data. These annotations, if explicitly preserved, could serve as powerful supervision signals for enhancing fine-grained vision-language alignment, a potential

that remains unexplored in the RS domain.

3. Multi-Granularity RS Image-Text Dataset

Unlike prior works that generate only global captions while discarding local object information [30, 31, 38, 52, 61], we explicitly preserve spatial and semantic details of individual geographical objects. Based on this, we propose MGRS-200k, the first RS image-text dataset designed for multi-granularity vision-language alignment.

MGRS-200k is constructed from 16 RS object detection datasets, sourced either from public data or generated using multiple foundation models on RS images. Conditioned on the RS images along with their corresponding object locations and categories, we employ Intern-VL3 [75] to generate/recaption detailed captions for each image. Inspired by recent studies [1, 10, 22, 59, 71] suggesting that longer and more detailed descriptions can benefit fine-grained alignment, we generate two types of captions for each image: a detailed but short caption and a long and more comprehensive caption. As a result, MGRS-200k contains about 200k RS images, each paired with both a short and a long global-level caption, as well as multiple object bbox-category pairs, in total, over one million instances.

We assess hallucinations within the dataset and demonstrate its reliability. We further show that our generated captions achieve significant improvements compared to existing RS datasets. Please refer to Appendix for details on data sources, caption generation, illustrative examples, data quality assessment, and additional ablation studies.

4. Fine-grained Image-Text Alignment in RS

Although fine-grained tuning methods for CLIP have proven effective in general domains, they often yield limited or negative transfer when applied to current RS data, as shown in Fig. 1. This motivates a systematic investigation into effective training strategies tailored for RS-specific fine-grained vision-language alignment. To this end, we conduct an in-depth analysis on two key aspects: *region-category alignment* and *local-global alignment*. The former directly aligns patch embeddings with text via region-text CL [20, 60], while the latter achieves indirect region-text alignment via local-global self-distillation [20, 54, 64]. In this section, we first present the overall architecture of our model, followed by the experimental setup, and finally delve into the two analytical perspectives outlined above. The overall analytical framework is illustrated in Fig. 2.

4.1. Model Architecture

Our model is built upon the CLIP architecture [45] for broad pre-trained model compatibility. Self-distillation that aligns global and local visual representations [54, 64] is employed to enhance fine-grained vision-language alignment. Specif-

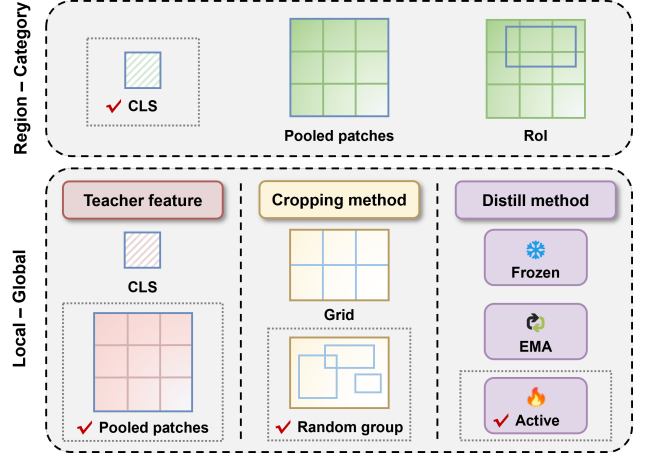


Figure 2. Overview of the analysis procedure. The item marked with a checkmark indicates the most effective method identified for RS-specific CLIP tuning.

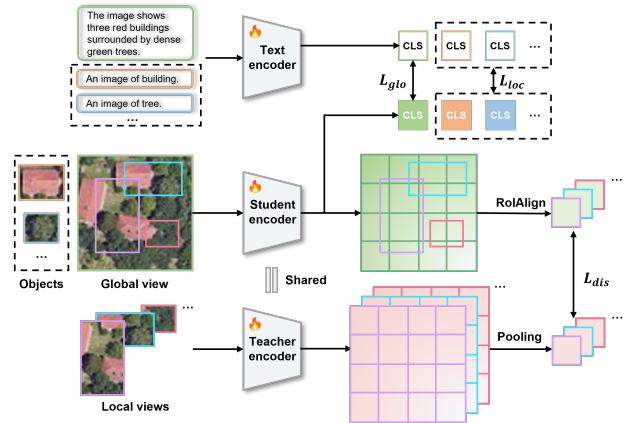


Figure 3. Architecture of FarSLIP. Stage one is trained on image-caption data with \mathcal{L}_{glo} and \mathcal{L}_{dis} , while stage two leverages image-caption and object-category pairs with \mathcal{L}_{glo} and \mathcal{L}_{loc} .

ically, we employ a teacher-student framework with two vision encoders sharing the same CLIP vision backbone. For image-text alignment, the student extracts image features to perform CL with text embeddings. For self-distillation, the input image is cropped into local views for the teacher, while the student processes the original full image. The features from the two encoders are then aligned through a local-global distillation loss. During inference, only the student encoder is used to extract visual features. An overview of the model is shown in Fig. 3, with its components described in detail in Sec. 4.3 and Sec. 4.4.

4.2. Experimental Setup

Model training. Our training data consists of the RS5M dataset [70], which provides image-caption pairs, and our

proposed MGRS-200k dataset, which contains both image-caption and region-category pairs. We use the short captions in MGRS-200k for image-text alignment.

For image-caption pairs, we follow CLIP and employ the standard InfoNCE loss to achieve global-level alignment between image and text embeddings. Specifically, the global loss for a batch of N image-text pairs is defined as:

$$\mathcal{L}_{\text{glo}} = \frac{1}{2} (\mathcal{L}_{I \rightarrow T} + \mathcal{L}_{T \rightarrow I}) \quad (1)$$

$$\mathcal{L}_{I \rightarrow T} = -\frac{1}{N} \sum_{i=1}^N \log \frac{\exp(S(V_i, T_i)/\tau)}{\sum_{j=1}^N \exp(S(V_i, T_j)/\tau)} \quad (2)$$

where V_i and T_i denote the image and text [CLS] embeddings of the i -th matched pair in a batch, respectively; the function $S(\cdot, \cdot)$ computes the cosine similarity between the embeddings; and τ is a learnable temperature.

For region-category pairs in the MGRS-200k dataset, the category labels are first converted into textual descriptions using a predefined template, such as ‘‘a satellite image of {category}’’. These descriptions are then used in the CL loss. However, since the same category often appears within a single image or across multiple samples, treating other samples with the same category as negative examples is semantically inappropriate. To address this, we adopt multi-positive CL (MPCL) [21, 47], where all region-category pairs sharing the same category are treated as positive matches. This allows the model to better capture the semantic consistency within each category. Specifically, the MPCL for a batch of M region-category pairs is defined as:

$$\mathcal{L}_{\text{loc}} = \frac{1}{2} (\mathcal{L}_{R \rightarrow C} + \mathcal{L}_{C \rightarrow R}) \quad (3)$$

$$\mathcal{L}_{R \rightarrow C} = \frac{1}{M} \sum_{i=1}^M -\frac{1}{|P(i)|} \sum_{j \in P(i)} \log \frac{\exp(S(V_i^r, T_j^c)/\tau)}{\sum_{k=1}^M \exp(S(V_i^r, T_k^c)/\tau)} \quad (4)$$

where V_i^r is the visual embedding of the i -th region; T_j^c is the textual [CLS] embedding of the j -th category; and the set $P(i)$ contains indices of positive samples sharing the same category as region i . The specific choice of visual embedding will be discussed in Sec. 4.3.

For the self-distillation process, the full image is passed through the student encoder. Given the bounding boxes of image crops, we apply RoIAlign [15] on the patch tokens to extract corresponding region-specific features, which we refer to as RoI features $\mathbf{p}_i^{\text{roi}}$. The local view, which is a cropped region from the original image, is fed into the teacher encoder to extract the corresponding local features $\mathbf{p}_i^{\text{local}}$. Then, the local features and the RoI features are used to calculate the distillation loss as follows.

$$\mathcal{L}_{\text{dis}} = \frac{1}{m} \sum_{i=1}^m \left(1 - \frac{\mathbf{p}_i^{\text{roi}} \cdot \mathbf{p}_i^{\text{local}}}{|\mathbf{p}_i^{\text{roi}}| |\mathbf{p}_i^{\text{local}}|} \right) \quad (5)$$

Our image and text encoders are initialized with the pre-trained weights from OpenAI CLIP [45]. More details about model training are provided in Appendix. Notably, we observe that when fine-tuned on RS image-text datasets, CLIP models based on ViT-L/14 consistently underperform those based on ViT-B/16. Therefore, we focus our experiments on ViT-B/16 and ViT-B/32 throughout this study.

Task, benchmark, and evaluation. Following prior works [31, 52], we evaluate global-level image-text alignment on eight RS scene classification datasets [9, 11, 16, 27, 34, 52, 56, 74], and three cross-modal retrieval datasets [35, 63, 65]. For local-level alignment evaluation, we employ eight RS semantic segmentation datasets [4, 7, 18, 19, 36, 51, 53, 58]. The evaluation metrics include Top-1 accuracy for ZSC, mean recall at R@1, R@5, and R@10 for cross-modal retrieval [31], and mIoU for OVSS. The implementation of OVSS follows recent training-free methods [29, 73], with the specific approach provided in Appendix. All reported results are averaged across the corresponding datasets.

4.3. Region-Category Alignment

Vision feature for CL. CLIP performs global alignment between image and text features, which introduces a gap when applied to dense prediction tasks such as OVSS, where region-level features are required. Recent works have proposed explicit region-text alignment to address this issue [20, 60], by aligning patch-level visual features (\mathbf{p}^{roi}) with textual CLS tokens via CL. But does direct region-text alignment remain effective when fine-tuning CLIP for RS?

Leveraging the region-category pairs in MGRS-200k, we compare three types of visual embeddings for region-category alignment using \mathcal{L}_{loc} : (1) the CLS token of the region image; (2) the average-pooled patch tokens of the region image; and (3) the RoI feature \mathbf{p}^{roi} , extracted from the global image patch tokens using RoIAlign over the region extent, following the method in FineCLIP [20].

Our findings differ significantly from those reported in FineCLIP, which benefits from more explicit region-text alignment. As shown in Tab. 1, RoI feature-based alignment leads to a notable performance drop compared to using CLS token, even underperforming the baseline. This trend consistently appears in both ZSC and OVSS tasks, even though OVSS is expected to benefit more from direct region-level supervision. A similar pattern is observed with pooled patch tokens: despite incorporating spatial cues, they still underperform on OVSS compared to CLS tokens.

To better understand this phenomenon, we investigate the models’ inherent capabilities. We argue that a VLFM with strong fine-grained understanding abilities should produce visual features with three properties: (1) clear feature boundaries, *i.e.*, high inter-class separation and low intra-

class variance; (2) accurate region-language alignment, *i.e.*, accurately assigning region features to their corresponding textual categories; and (3) high semantic coherence, *i.e.*, pixels with similar content should have similar features. To quantify these abilities, we use the Davies-Bouldin Index (DBI) [12] to indicate feature discriminability, compute top-1 accuracy (Acc@1) of instance features against text queries to represent region-text alignment, and calculate the mean average precision (mAP) of feature similarity across pixels to reflect semantic coherence. Details of the computation of these metrics are provided in the appendix.

We compare the analysis metrics of region-text alignment using RoI features and CLS tokens, as shown in Tab. 2. Thanks to RS-specific fine-tuning, both approaches improve the model’s feature discriminability and region-language alignment, as reflected by the increased DBI and Acc@1. The RoI-based method performs slightly better, due to its more explicit instance-level training. However, this approach significantly reduces the model’s semantic coherence, which is critical for fine-grained understanding [26, 42, 55], thereby leading to worse OVSS performance. In comparison, CLS token-based training not only preserves the improved feature discriminability and region-text alignment but also enhances semantic coherence, which is one of the inherent properties of CLIP [26, 73]. Additional qualitative analyses can be found in the appendix.

Takeaway 1: A more suitable approach is to preserve CLIP’s original visual-language association, *i.e.*, aligning via the CLS token, while leveraging its inherent spatial awareness for RS OVSS [50, 73].

Table 1. Comparison of region visual feature types under \mathcal{L}_{loc} -only training on MGRS-200k (baseline: CLIP).

Region feat.	ViT-B/16		ViT-B/32	
	ZSC	OVSS	ZSC	OVSS
Baseline	50.60	34.52	43.10	29.32
RoI embedding	45.43	30.42	42.86	26.37
Pooled patches	48.12	28.89	45.44	26.69
CLS token	58.69	35.42	57.02	29.38

Effectiveness of region-category pairs. Unlike prior works that discard local information when generating global captions for RS images, we investigate the effect of retaining region-category pairs during dataset construction. As Tab. 3 shows, applying region-category CL significantly improves ZSC performance over using global image-caption CL. It also brings accuracy gains for OVSS on ViT-B/16, though a slight drop is observed on ViT-B/32, possibly due to small regions in the training dataset combined with

Table 2. Accuracy improvement percentages (unit: %) over the baseline for different training methods. The first two rows show the relative changes achieved by fine-tuning with different region-category alignment methods compared to CLIP. The last two rows show the relative changes obtained by using different self-distillation methods versus no self-distillation.

Objective	Method	DBI	Acc@1	mAP
Region-cat. align.	RoI embedding	+21.8	+1.1	-1.5
	CLS token	+18.3	+0.5	+1.2
Self-distillation	RoI-to-CLS	+0.9	-3.9	-1.2
	RoI-to-Pooled	+6.1	-0.6	-0.2

Table 3. Comparison of different loss configurations on models fine-tuned with the MGRS-200k dataset.

\mathcal{L}_{glo}	\mathcal{L}_{loc}	ViT-B/16		ViT-B/32	
		ZSC	OVSS	ZSC	OVSS
✓		56.92	35.23	54.04	30.64
	✓	58.69	35.42	57.02	29.38
✓	✓	59.17	35.67	58.34	30.56

coarse patch features. Nevertheless, combining \mathcal{L}_{glo} and \mathcal{L}_{loc} losses yields the best overall performance, highlighting the value of preserving region-category pairs when constructing RS image-text datasets.

Takeaway 2: Future RS image-text data generation should explicitly retain fine-grained supervision signals that previous RS datasets have underutilized.

4.4. Local-Global Alignment

As self-distillation has been proven effective in indirectly enhancing region-text alignment through local-global distillation on top of CLIP, we conduct an in-depth analysis of its effectiveness for RS-specific tuning. We primarily use the RS5M dataset [70] for the analysis, as its relatively large scale allows for more reliable conclusions. To analyze the effect of different data scales, we randomly sample two subsets: 0.5M and 2.5M image-text pairs. To balance data volume and experimental efficiency, experiments are conducted using the 2.5M subset unless otherwise specified.

What to distill? We investigate which teacher representations should be transferred to the student for effective self-distillation, focusing on selecting appropriate local representations and how to generate local views.

While prior studies demonstrate that self-distillation by aligning RoI features with cropped images’ CLS tokens greatly enhances local-level vision-language alignment [20, 54, 64], our experiments reveal an unexpected inconsis-

tency. As shown in Tab. 4, CLS token-based self-distillation results in a noticeable performance drop in both ZSC and OVSS, which is surprising, particularly given the decline in OVSS accuracy, contradicting existing findings [20, 54, 64].

To further understand this phenomenon, we find that CLS-token-based self-distillation slightly improves feature discriminability (Tab. 2), but largely degrades region-text alignment and semantic coherence. This can be attributed to the nature of RS imagery: large spatial coverage, small targets, and highly heterogeneous scenes. We observe that the CLS token often corresponds to the dominant regions in RS images (see appendix for visualizations). In this case, aligning CLS tokens with RoI features leads the model to learn patch-level representations biased toward these dominant regions, while neglecting numerous non-dominant areas, thereby hindering fine-grained feature extraction.

To enable effective local-global self-distillation, we propose patch-to-patch distillation. Specifically, as shown in Fig. 3, we extract average-pooled patch embeddings from cropped images to perform patch-to-patch self-distillation. This method has three advantages: (1) it aligns patch features with the content of their own crop views, thereby reducing background interference [44]; (2) it aligns patch features with higher-resolution representations extracted by the teacher model, improving precision [13, 29]; and (3) both views are derived from fine-grained patch features that preserve detailed scene information, avoiding information loss caused by the discriminative nature of the CLS token [20, 54]. Table 4 shows that this method is far more effective than CLS token-based distillation and improves results on both ZSC and OVSS tasks. It also leads to better feature discriminability while preserving semantic coherence, as evidenced in Tab. 2.

Regarding the generation of local views, we compare two strategies: grid sampling [54, 64] and random cropping [44]. As shown in Tab. 4, random cropping is a better local view generation method in this context, demonstrated by higher OVSS accuracy and competitive ZSC performance.

Takeaway 3: Patch-to-patch self-distillation is superior to CLS-to-patch, which tends to constrain patch features to dominant categories and lose visual details.

How to distill? An effective distillation strategy enables the student model to better absorb the teacher’s knowledge. While existing works adopt the frozen CLIP vision encoder as the teacher [44, 54, 64] to leverage its powerful pre-trained representations, and freeze the text encoder during distillation to improve training stability [54], our findings once again reveal a different perspective for RS-specific adaptation.

We test frozen-teacher distillation on an RS-specific CLIP variant trained with \mathcal{L}_{glo} (Tab. 5), where performance

Table 4. Comparison of distillation features and cropping methods. RC = random crop; CLS / pooled = CLS token / pooled patch token.

Distill feat. / Crop method	ViT-B/16		ViT-B/32	
	ZSC	OVSS	ZSC	OVSS
Without Distillation	64.13	36.34	62.22	31.66
RoI-to-CLS / RC	63.05	35.21	62.31	30.28
RoI-to-Pooled / Grid	65.19	35.88	62.37	31.06
RoI-to-Pooled / RC	64.91	37.22	62.31	32.25

Table 5. Comparison of different teacher encoder update strategies for self-distillation.

Distill method	ViT-B/16		ViT-B/32	
	ZSC	OVSS	ZSC	OVSS
Baseline	64.13	36.34	62.22	31.66
Frozen	61.05	36.44	58.57	26.64
EMA	63.16	35.84	61.60	31.52
Online	64.91	37.22	62.31	32.25

drops significantly in most cases compared to the baseline. Additionally, we evaluate updating the teacher via EMA, a technique widely adopted in self-supervised learning for its training stability [42]. Nevertheless, the performance remains unsatisfactory. In contrast, online distillation [20], where the teacher and student are trained simultaneously, enables more effective knowledge transfer, as evidenced by its superior accuracy in Tab. 5.

For the text encoder, Tab. 6 shows that freezing it during training limits performance gains. One possible explanation is that the CLIP text encoder lacks sufficient understanding of RS domain language and needs further fine-tuning to better capture domain-specific terms and semantics.

Takeaway 4: When fine-tuning CLIP to the novel domain of RS with self-distillation, unfreezing both the vision and text encoders results in better performance.

Table 6. Comparison of freezing vs. unfreezing the text encoder during self-distillation. Grid cropping is used for local view generation, consistent with [54].

Frozen text encoder	ViT-B/16		ViT-B/32	
	ZSC	OVSS	ZSC	OVSS
Baseline	64.13	36.34	62.22	31.66
Frozen	62.48	34.30	59.80	29.47
Unfrozen	65.19	35.88	62.37	31.06

When to distill? We further investigate the effectiveness of patch-to-patch self-distillation under different scenarios, especially with varying data conditions. In the case of data scale, as shown in Tab. 7, it consistently improves performance in both ZSC and OVSS across nearly all dataset scales and backbones, demonstrating the effectiveness and robustness. Notably, the model trained on the 2.5M dataset with self-distillation outperforms the model trained on the 5M dataset without distillation, further demonstrating the benefit of patch-to-patch self-distillation. In most cases, the highest accuracy is consistently achieved by models trained on the largest dataset combined with self-distillation. The only exception is the ViT-B/32 OVSS setting, where performance on the 5M dataset is lower than on the 2.5M dataset. However, even without distillation (using only \mathcal{L}_{glo}), the model trained on the 5M dataset still underperforms the one trained on the 2.5M dataset. Therefore, this degradation can be attributed to data-related issues, indicating that when the dataset itself provides poor image-text alignment, applying distillation may harm performance.

We then investigate the impact of self-distillation on the MGRS-200k dataset under two baselines: (1) \mathcal{L}_{glo} only, and (2) $\mathcal{L}_{\text{glo}} + \mathcal{L}_{\text{loc}}$. As shown in Tab. 8, adding distillation to the \mathcal{L}_{glo} -only baseline (first vs. second row) brings modest improvements overall, though a slight performance drop is observed for OVSS with the ViT-B/32 backbone. This is likely because self-distillation benefits more from ViT-B/16, which offers higher-resolution patch features. When applied on top of the $\mathcal{L}_{\text{glo}} + \mathcal{L}_{\text{loc}}$ baseline (third vs. fourth row), which is already strong under fine-grained supervision, self-distillation generally has limited effect, bringing only minor improvement with the ViT-B/16 backbone. This suggests that sufficient region-text supervision may reduce the benefits of additional self-distillation.

Table 7. Comparison of performance with (✓) and without (✗) self-distillation (\mathcal{L}_{dis}) on top of image-caption CL (\mathcal{L}_{glo}) across different data scales and backbones. The hyperparameters are tuned based on the no-distill cases to ensure a fair evaluation of the impact of distillation. Bold and underlined values indicate the best and second-best performance, respectively.

Data scale	Distill	ViT-B/16		ViT-B/32	
		ZSC	OVSS	ZSC	OVSS
RS5M-0.5M	✗	61.96	36.06	60.43	31.69
	✓	62.60	36.23	61.54	<u>31.87</u>
RS5M-2.5M	✗	64.13	36.34	62.22	31.66
	✓	<u>64.91</u>	<u>37.22</u>	<u>62.31</u>	32.25
RS5M-5M	✗	64.76	36.57	62.16	31.53
	✓	65.79	37.30	62.84	31.29

Table 8. Ablation study of \mathcal{L}_{dis} , under \mathcal{L}_{glo} -only and combined \mathcal{L}_{glo} and \mathcal{L}_{loc} supervision. Training dataset: MGRS-200k.

\mathcal{L}_{glo}	\mathcal{L}_{loc}	\mathcal{L}_{dis}	ViT-B/16		ViT-B/32	
			ZSC	OVSS	ZSC	OVSS
✓			56.63	35.19	54.28	30.61
✓		✓	57.39	35.78	54.58	30.16
✓	✓		58.62	35.61	57.88	30.28
✓	✓	✓	58.79	35.63	57.83	30.20

Table 9. Comparison of cross-modal retrieval accuracies of different RS-specific CLIP variants across multiple benchmarks. * indicates models trained with in-hold supervision.

Backbone	Method	RSICD		RSITMD		UCM	
		I2T	T2I	I2T	T2I	I2T	T2I
ViT-B/32	CLIP	16.3	12.8	24.7	22.4	53.2	42.5
	RemoteCLIP*	33.7	28.1	45.7	42.8	77.1	73.5
	SkyCLIP	21.2	19.7	29.1	30.1	66.7	58.7
	GeoRSCLIP	26.3	22.0	<u>32.5</u>	31.9	<u>67.9</u>	61.5
	FarSLIP-s1	25.9	21.7	31.3	32.8	67.5	59.7
	FarSLIP-s2	<u>26.8</u>	<u>25.0</u>	31.9	<u>35.3</u>	67.8	<u>67.0</u>
ViT-B/16	CLIP	19.8	13.4	22.9	23.4	61.4	47.5
	LRSClip*	29.7	26.3	39.4	<u>33.1</u>	79.5	68.7
	GeoRSCLIP	27.0	21.7	34.0	32.8	68.6	<u>62.6</u>
	FarSLIP-s1	27.4	21.9	33.6	32.9	69.4	61.7
	FarSLIP-s2	<u>27.4</u>	<u>23.7</u>	33.5	34.5	<u>70.6</u>	62.2

5. FarSLIP: A Family of RS VLFM

Based on the above insights, we propose a new RS-specific VLFM named FarSLIP (Fig. 3), trained in a two-stage manner. In stage one (FarSLIP-s1), the model is trained with both \mathcal{L}_{glo} and \mathcal{L}_{dis} , using the RS5M dataset for ViT-B/16 and RS5M-2.5M subset for ViT-B/32. We adopt patch-to-patch self-distillation with random crops to generate local views, and unfreeze both the teacher and student vision encoders as well as the text encoder. In stage two (FarSLIP-s2), the model is further fine-tuned on the MGRS-200k dataset using \mathcal{L}_{glo} and \mathcal{L}_{loc} . The entire training process employs full-parameter fine-tuning, initialized from OpenAI CLIP. Detailed settings are provided in Appendix.

We compare FarSLIP with several RS-specific VLFMs (when their models are publicly available) and general-domain VLFMs equipped with fine-grained vision-language alignment capabilities. Tab. 10 and Tab. 11 report OVSS and ZSC results, respectively. FarSLIP-s1 achieves competitive or best performance across all benchmarks and outperforms other VLFMs in mean accuracy, demonstrating its strength in both global and fine-grained understanding. FarSLIP-s2, further fine-tuned on our proposed MGRS-

Table 10. OVSS accuracies across RS benchmarks (mIoU, %). *G* denotes general-domain models, while *RS* refers to RS-specific models. *f*. indicates models specifically designed with fine-grained optimization. All models use an input image size of 224, except TIPS (448).

Backbone	Method	Domain	OEM	LoveDA	Potsdam	Vaihingen	UDD5	VDD	UAvid	iSAID	Mean
ViT-B/32	CLIP [45]	G	24.39	25.52	37.13	25.52	35.63	35.05	28.46	6.69	27.30
	MetaCLIP [62]	G	24.24	26.38	35.90	20.90	31.82	30.06	29.77	7.27	25.79
	RemoteCLIP [31]	RS	18.28	33.62	21.44	21.57	29.64	29.19	17.28	<u>14.79</u>	23.23
	SkyCLIP [52]	RS	23.59	29.45	40.68	23.16	34.94	30.68	28.78	3.03	26.79
	GeoRSCLIP [70]	RS	32.49	27.20	36.30	22.41	33.16	35.22	29.80	9.81	28.30
	FarSLIP1	RS / f.	<u>28.29</u>	30.04	36.28	22.83	36.80	<u>37.23</u>	<u>31.42</u>	16.09	<u>29.87</u>
	FarSLIP2	RS / f.	26.66	<u>30.79</u>	40.38	<u>24.33</u>	<u>36.77</u>	38.54	32.82	13.66	30.49
ViT-B/14	TIPS (448) [37]	G / f.	36.56	24.68	35.30	25.29	44.57	42.58	43.19	4.66	32.10
ViT-B/16	CLIP [45]	G	31.89	29.62	42.63	27.31	41.54	39.20	36.83	9.24	32.28
	MetaCLIP [62]	G	33.43	24.86	37.39	20.20	37.26	31.25	32.63	6.82	27.98
	CLIPSelf [54]	G / f.	12.61	18.36	6.27	5.51	18.44	19.99	15.80	5.22	12.78
	FineCLIP [20]	G / f.	24.01	20.82	29.62	17.41	34.53	33.86	26.69	6.54	24.19
	COSMOS [22]	G / f.	21.90	26.16	31.23	21.57	35.90	30.86	26.38	5.91	24.99
	LRSLIP [6]	RS	30.75	34.61	43.98	26.68	44.24	37.90	37.57	10.11	33.23
	GeoRSCLIP [70]	RS	<u>35.26</u>	34.10	45.52	<u>23.35</u>	43.22	40.57	39.13	13.56	34.34
	FarSLIP1	RS / f.	35.89	33.59	<u>46.50</u>	22.34	<u>44.60</u>	<u>40.63</u>	40.23	19.76	35.44
	FarSLIP2	RS / f.	34.39	<u>34.23</u>	47.48	22.81	44.83	40.82	<u>40.03</u>	<u>18.67</u>	<u>35.41</u>

Table 11. Comparison of ZSC accuracies (Top-1 acc., %) of different RS-specific CLIP variants across multiple benchmarks.

Backbone	Method	SkyScript	AID	EuroSAT	FMoW	MillionAID	PatternNet	NWPU	RSICB	Mean
ViT-B/32	CLIP [45]	32.37	58.00	22.00	15.61	51.62	52.97	54.82	29.92	39.66
	RemoteCLIP [31]	27.67	88.10	28.52	11.15	45.50	55.95	69.10	43.91	46.24
	SkyCLIP [52]	<u>52.92</u>	70.90	33.33	19.23	62.72	72.19	66.63	46.20	53.02
	GeoRSCLIP [70]	51.92	69.75	41.33	37.14	<u>71.60</u>	<u>77.00</u>	<u>69.90</u>	<u>46.93</u>	58.20
	FarSLIP-s1	51.51	<u>73.80</u>	<u>49.26</u>	<u>34.49</u>	69.42	74.69	69.93	46.00	<u>58.64</u>
	FarSLIP-s2	53.79	73.30	49.30	30.12	72.05	80.45	67.77	54.17	60.12
ViT-B/16	CLIP [45]	42.60	65.85	32.78	19.85	53.37	63.82	62.25	33.56	46.76
	LRSLIP [6]	55.73	69.75	44.52	22.66	<u>67.76</u>	77.89	74.28	54.75	58.42
	GeoRSCLIP [70]	55.33	72.15	54.59	34.50	67.27	78.75	72.32	52.75	60.96
	FarSLIP-s1	<u>56.19</u>	<u>73.30</u>	59.81	<u>34.60</u>	66.82	<u>78.85</u>	<u>72.72</u>	52.80	<u>61.89</u>
	FarSLIP-s2	57.98	73.95	<u>55.52</u>	35.86	68.04	80.82	71.49	<u>54.24</u>	62.24

200k dataset (which is fully out-of-distribution relative to the adopted benchmarks), brings additional improvements and achieves the highest overall performance. We further evaluate cross-modal retrieval performance of FarSLIP, as shown in Tab. 9. Excluding models trained on hold-in data, FarSLIP achieves either SOTA or competitive results.

6. Conclusion

This study explores fine-grained adaption of CLIP for RS domain. With our proposed MGRS-200k dataset, constructed from public resources, we demonstrate that current RS image-text data generation paradigms often underutilize valuable region-level information, which can in fact provide

effective supervision for both global- and local-level vision-language alignment. Our findings offer practical guidance for future RS vision-language data construction.

Furthermore, we conduct an in-depth investigation of existing fine-grained CLIP fine-tuning strategies and show that current region-language alignment approaches can undermine semantic coherence, thereby degrading performance on fine-grained RS interpretation tasks. By applying appropriate training objectives, including patch-to-patch self-distillation and basic CLS token-based region-category CL, we achieve a SOTA VLFM specialized for RS. We hope that this study can provide valuable insights for fine-grained adaptation of CLIP to downstream domains.

References

- [1] Mothilal Asokan, Kebin Wu, and Fatima Albreiki. Finelip: Extending clip’s reach via fine-grained alignment with longer text inputs. In *Proceedings of the Computer Vision and Pattern Recognition Conference*, pages 14495–14504, 2025. 2, 3
- [2] Luca Barsellotti, Lorenzo Bianchi, Nicola Messina, Fabio Carrara, Marcella Cornia, Lorenzo Baraldi, Fabrizio Falchi, and Rita Cucchiara. Talking to dino: Bridging self-supervised vision backbones with language for open-vocabulary segmentation. In *Proceedings of the IEEE/CVF International Conference on Computer Vision*, pages 22025–22035, 2025. 1
- [3] Ioana Bica, Anastasija Ilić, Matthias Bauer, Goker Erdogan, Matko Bošnjak, Christos Kaplanis, Alexey A. Gritsenko, Matthias Minderer, Charles Blundell, Razvan Paşcanu, and Jovana Mitrović. Improving fine-grained understanding in image-text pre-training. In *Proceedings of the 41st International Conference on Machine Learning*, 2024. 1, 2
- [4] Wenxiao Cai, Ke Jin, Jinyan Hou, Cong Guo, Letian Wu, and Wankou Yang. Vdd: Varied drone dataset for semantic segmentation. *Journal of Visual Communication and Image Representation*, 109:104429, 2025. 4
- [5] Hong-You Chen, Zhengfeng Lai, Haotian Zhang, Xinze Wang, Marcin Eichner, Keen You, Meng Cao, Bowen Zhang, Yinfei Yang, and Zhe Gan. Contrastive localized language-image pre-training. *arXiv preprint arXiv:2410.02746*, 2024. 1, 2
- [6] Weizhi Chen, Jingbo Chen, Yupeng Deng, Jiansheng Chen, Yuman Feng, Zhihao Xi, Diyou Liu, Kai Li, and Yu Meng. Lrsclip: A vision-language foundation model for aligning remote sensing image with longer text. *arXiv preprint arXiv:2503.19311*, 2025. 8
- [7] Yu Chen, Yao Wang, Peng Lu, Yisong Chen, and Guoping Wang. Large-scale structure from motion with semantic constraints of aerial images. In *Chinese Conference on Pattern Recognition and Computer Vision (PRCV)*, pages 347–359. Springer, 2018. 4
- [8] Gong Cheng, Junwei Han, Peicheng Zhou, and Lei Guo. Multi-class geospatial object detection and geographic image classification based on collection of part detectors. *ISPRS Journal of Photogrammetry and Remote Sensing*, 98: 119–132, 2014. 3
- [9] Gong Cheng, Junwei Han, and Xiaoqiang Lu. Remote sensing image scene classification: Benchmark and state of the art. *Proceedings of the IEEE*, 105(10):1865–1883, 2017. 4, 3
- [10] Hyungyu Choi, Young Kyun Jang, and Chanho Eom. Goal: Global-local object alignment learning. In *Proceedings of the Computer Vision and Pattern Recognition Conference*, pages 4070–4079, 2025. 3, 2
- [11] Gordon Christie, Neil Fendley, James Wilson, and Ryan Mukherjee. Functional map of the world. In *Proceedings of the IEEE Conference on Computer Vision and Pattern Recognition*, pages 6172–6180, 2018. 4
- [12] David L Davies and Donald W Bouldin. A cluster separation measure. *IEEE transactions on pattern analysis and machine intelligence*, (2):224–227, 2009. 5
- [13] Stephanie Fu, Mark Hamilton, Laura E. Brandt, Axel Feldmann, Zhoutong Zhang, and William T. Freeman. Featup: A model-agnostic framework for features at any resolution. In *The Twelfth International Conference on Learning Representations*, 2024. 6
- [14] Sachin Goyal, Ananya Kumar, Sankalp Garg, Zico Kolter, and Aditi Raghunathan. Finetune like you pretrain: Improved finetuning of zero-shot vision models. In *Proceedings of the IEEE/CVF Conference on Computer Vision and Pattern Recognition*, pages 19338–19347, 2023. 1
- [15] Kaiming He, Georgia Gkioxari, Piotr Dollár, and Ross Girshick. Mask r-cnn. In *Proceedings of the IEEE international conference on computer vision*, pages 2961–2969, 2017. 4
- [16] Patrick Helber, Benjamin Bischke, Andreas Dengel, and Damian Borth. Eurosat: A novel dataset and deep learning benchmark for land use and land cover classification. *IEEE Journal of Selected Topics in Applied Earth Observations and Remote Sensing*, 12(7):2217–2226, 2019. 4
- [17] Meng-Ru Hsieh, Yen-Liang Lin, and Winston H Hsu. Drone-based object counting by spatially regularized regional proposal network. In *Proceedings of the IEEE international conference on computer vision*, pages 4145–4153, 2017. 3
- [18] ISPRS. 2D Semantic Labeling Contest - Potsdam Dataset. <https://www.isprs.org/resources/datasets/benchmarks/UrbanSemLab/2d-sem-label-potsdam.aspx>, 2016. Accessed: 2025-07-31. 4
- [19] ISPRS. 2D Semantic Labeling Contest - Vaihingen Dataset. <https://www.isprs.org/resources/datasets/benchmarks/UrbanSemLab/2d-sem-label-vaihingen.aspx>, 2016. Accessed: 2025-07-31. 4
- [20] Dong Jing, Xiaolong He, Yutian Luo, Nanyi Fei, Wei Wei, Huiwen Zhao, Zhiwu Lu, et al. Fineclip: Self-distilled region-based clip for better fine-grained understanding. *Advances in Neural Information Processing Systems*, 37:27896–27918, 2024. 2, 3, 4, 5, 6, 8
- [21] Prannay Khosla, Piotr Teterwak, Chen Wang, Aaron Sarna, Yonglong Tian, Phillip Isola, Aaron Maschinot, Ce Liu, and Dilip Krishnan. Supervised contrastive learning. *Advances in neural information processing systems*, 33:18661–18673, 2020. 4
- [22] Sanghwan Kim, Rui Xiao, Mariana-Iuliana Georgescu, Stephan Alaniz, and Zeynep Akata. Cosmos: Cross-modality self-distillation for vision language pre-training. In *Proceedings of the Computer Vision and Pattern Recognition Conference*, pages 14690–14700, 2025. 2, 3, 8
- [23] Ananya Kumar, Aditi Raghunathan, Robbie Jones, Tengyu Ma, and Percy Liang. Fine-tuning can distort pretrained features and underperform out-of-distribution. *arXiv preprint arXiv:2202.10054*, 2022. 1
- [24] Darius Lam, Richard Kuzma, Kevin McGee, Samuel Doolley, Michael Laielli, Matthew Klaric, Yaroslav Bulatov, and Brendan McCord. xvview: Objects in context in overhead imagery. *arXiv preprint arXiv:1802.07856*, 2018. 3

- [25] Mengcheng Lan, Chaofeng Chen, Yiping Ke, Xinjiang Wang, Litong Feng, and Wayne Zhang. Clearclip: Decomposing clip representations for dense vision-language inference. In *European Conference on Computer Vision*, pages 143–160. Springer, 2024. 1
- [26] Mengcheng Lan, Chaofeng Chen, Yiping Ke, Xinjiang Wang, Litong Feng, and Wayne Zhang. Proxycip: Proxy attention improves clip for open-vocabulary segmentation. In *European Conference on Computer Vision*, pages 70–88. Springer, 2024. 1, 2, 5
- [27] Haifeng Li, Xin Dou, Chao Tao, Zhixiang Wu, Jie Chen, Jian Peng, Min Deng, and Ling Zhao. Rsi-cb: A large-scale remote sensing image classification benchmark using crowd-sourced data. *Sensors*, 20(6):1594, 2020. 4
- [28] Ke Li, Gang Wan, Gong Cheng, Liqiu Meng, and Junwei Han. Object detection in optical remote sensing images: A survey and a new benchmark. *ISPRS journal of photogrammetry and remote sensing*, 159:296–307, 2020. 3
- [29] Kaiyu Li, Ruixun Liu, Xiangyong Cao, Xueru Bai, Feng Zhou, Deyu Meng, and Zhi Wang. Segearth-ov: Towards training-free open-vocabulary segmentation for remote sensing images. In *Proceedings of the Computer Vision and Pattern Recognition Conference*, pages 10545–10556, 2025. 1, 4, 6
- [30] Zhenshi Li, Dilxat Muhtar, Feng Gu, Yanglangxing He, Xueliang Zhang, Pengfeng Xiao, Guangjun He, and Xiaoxiang Zhu. Lhrs-bot-nova: Improved multimodal large language model for remote sensing vision-language interpretation. *ISPRS Journal of Photogrammetry and Remote Sensing*, 227:539–550, 2025. 2, 3
- [31] Fan Liu, DeLong Chen, Zhangqingyun Guan, Xiaocong Zhou, Jiale Zhu, Qiaolin Ye, Liyong Fu, and Jun Zhou. Remoteclip: A vision language foundation model for remote sensing. *IEEE Transactions on Geoscience and Remote Sensing*, 62:1–16, 2024. 1, 2, 3, 4, 8
- [32] Zikun Liu, Liu Yuan, Lubin Weng, and Yiping Yang. A high resolution optical satellite image dataset for ship recognition and some new baselines. In *International conference on pattern recognition applications and methods*, pages 324–331. SciTePress, 2017. 3
- [33] Yang Long, Yiping Gong, Zhifeng Xiao, and Qing Liu. Accurate object localization in remote sensing images based on convolutional neural networks. *IEEE Transactions on Geoscience and Remote Sensing*, 55(5):2486–2498, 2017. 3
- [34] Yang Long, Gui-Song Xia, Shengyang Li, Wen Yang, Michael Ying Yang, Xiao Xiang Zhu, Liangpei Zhang, and Deren Li. On creating benchmark dataset for aerial image interpretation: Reviews, guidances, and million-aid. *IEEE Journal of selected topics in applied earth observations and remote sensing*, 14:4205–4230, 2021. 4
- [35] Xiaoqiang Lu, Binqiang Wang, Xiangtao Zheng, and Xuelong Li. Exploring models and data for remote sensing image caption generation. *IEEE Transactions on Geoscience and Remote Sensing*, 56(4):2183–2195, 2017. 4
- [36] Ye Lyu, George Vosselman, Gui-Song Xia, Alper Yilmaz, and Michael Ying Yang. Uavid: A semantic segmentation dataset for uav imagery. *ISPRS journal of photogrammetry and remote sensing*, 165:108–119, 2020. 4
- [37] Kevis-Kokitsi Maninis, Kaifeng Chen, Soham Ghosh, Arjun Karapur, Koert Chen, Ye Xia, Bingyi Cao, Daniel Salz, Guangxing Han, Jan Dlabal, et al. Tips: Text-image pretraining with spatial awareness. *arXiv preprint arXiv:2410.16512*, 2024. 2, 8
- [38] Dilxat Muhtar, Zhenshi Li, Feng Gu, Xueliang Zhang, and Pengfeng Xiao. Lhrs-bot: Empowering remote sensing with vgi-enhanced large multimodal language model. In *European Conference on Computer Vision*, pages 440–457. Springer, 2024. 2, 3
- [39] Jishnu Mukhoti, Yarin Gal, Philip HS Torr, and Puneet K Dokania. Fine-tuning can cripple your foundation model; preserving features may be the solution. *arXiv preprint arXiv:2308.13320*, 2023. 1
- [40] Jishnu Mukhoti, Tsung-Yu Lin, Omid Poursaeed, Rui Wang, Ashish Shah, Philip HS Torr, and Ser-Nam Lim. Open vocabulary semantic segmentation with patch aligned contrastive learning. In *Proceedings of the IEEE/CVF Conference on Computer Vision and Pattern Recognition*, pages 19413–19423, 2023. 1, 2
- [41] Muhammad Ferjad Naeem, Yongqin Xian, Xiaohua Zhai, Lukas Hoyer, Luc Van Gool, and Federico Tombari. Silc: Improving vision language pretraining with self-distillation. In *European Conference on Computer Vision*, pages 38–55. Springer, 2024. 2
- [42] Maxime Oquab, Timothée Darcet, Théo Moutakanni, Huy V. Vo, Marc Szafraniec, Vasil Khalidov, Pierre Fernandez, Daniel HAZIZA, Francisco Massa, Alaaeldin El-Nouby, Mido Assran, Nicolas Ballas, Wojciech Galuba, Russell Howes, Po-Yao Huang, Shang-Wen Li, Ishan Misra, Michael Rabbat, Vasu Sharma, Gabriel Synnaeve, Hu Xu, Herve Jegou, Julien Mairal, Patrick Labatut, Armand Joulin, and Piotr Bojanowski. DINOv2: Learning robust visual features without supervision. *Transactions on Machine Learning Research*, 2024. 2, 5, 6
- [43] Jiancheng Pan, Yanxing Liu, Yuqian Fu, Muyuan Ma, Jiahao Li, Danda Pani Paudel, Luc Van Gool, and Xiaomeng Huang. Locate anything on earth: Advancing open-vocabulary object detection for remote sensing community. In *Proceedings of the AAAI Conference on Artificial Intelligence*, pages 6281–6289, 2025. 2, 3
- [44] Congpei Qiu, Yanhao Wu, Wei Ke, Xiuxiu Bai, and Tong Zhang. Refining CLIP’s spatial awareness: A visual-centric perspective. In *The Thirteenth International Conference on Learning Representations*, 2025. 2, 6
- [45] Alec Radford, Jong Wook Kim, Chris Hallacy, Aditya Ramesh, Gabriel Goh, Sandhini Agarwal, Girish Sastry, Amanda Askell, Pamela Mishkin, Jack Clark, et al. Learning transferable visual models from natural language supervision. In *International conference on machine learning*, pages 8748–8763. PmLR, 2021. 1, 3, 4, 8, 2
- [46] Xian Sun, Peijin Wang, Zhiyuan Yan, Feng Xu, Ruiping Wang, Wenhui Diao, Jin Chen, Jihao Li, Yingchao Feng, Tao Xu, et al. Fair1m: A benchmark dataset for fine-grained object recognition in high-resolution remote sensing imagery. *ISPRS Journal of Photogrammetry and Remote Sensing*, 184:116–130, 2022. 3

- [47] Yonglong Tian, Lijie Fan, Phillip Isola, Huiwen Chang, and Dilip Krishnan. Stablerep: Synthetic images from text-to-image models make strong visual representation learners. *Advances in Neural Information Processing Systems*, 36: 48382–48402, 2023. 4
- [48] Michael Tschannen, Alexey Gritsenko, Xiao Wang, Muhammad Ferjad Naeem, Ibrahim Alabdulmohsin, Nikhil Parthasarathy, Talfan Evans, Lucas Beyer, Ye Xia, Basil Mustafa, et al. Siglip 2: Multilingual vision-language encoders with improved semantic understanding, localization, and dense features. *arXiv preprint arXiv:2502.14786*, 2025. 2
- [49] Stéphane Vujasinović, Stefan Becker, Timo Breuer, Sebastian Bullinger, Norbert Scherer-Negenborn, and Michael Arens. Integration of the 3d environment for uav onboard visual object tracking. *Applied Sciences*, 10(21):7622, 2020. 3
- [50] Feng Wang, Jieru Mei, and Alan Yuille. Sclip: Rethinking self-attention for dense vision-language inference. In *European Conference on Computer Vision*, pages 315–332. Springer, 2024. 1, 5
- [51] Junjue Wang, Zhuo Zheng, Ailong Ma, Xiaoyan Lu, and Yanfei Zhong. Loveda: A remote sensing land-cover dataset for domain adaptive semantic segmentation. *arXiv preprint arXiv:2110.08733*, 2021. 4
- [52] Zhecheng Wang, Rajanie Prabha, Tianyuan Huang, Jiajun Wu, and Ram Rajagopal. Skyscript: A large and semantically diverse vision-language dataset for remote sensing. In *Proceedings of the AAAI Conference on Artificial Intelligence*, pages 5805–5813, 2024. 1, 2, 3, 4, 8
- [53] Syed Waqas Zamir, Aditya Arora, Akshita Gupta, Salman Khan, Guolei Sun, Fahad Shahbaz Khan, Fan Zhu, Ling Shao, Gui-Song Xia, and Xiang Bai. isaid: A large-scale dataset for instance segmentation in aerial images. In *Proceedings of the IEEE/CVF conference on computer vision and pattern recognition workshops*, pages 28–37, 2019. 4
- [54] Size Wu, Wenwei Zhang, Lumin Xu, Sheng Jin, Xiangtai Li, Wentao Liu, and Chen Change Loy. CLIPSelf: Vision transformer distills itself for open-vocabulary dense prediction. In *The Twelfth International Conference on Learning Representations*, 2024. 1, 2, 3, 5, 6, 8
- [55] Monika Wysoczańska, Oriane Siméoni, Michaël Ramamonjisoa, Andrei Bursuc, Tomasz Trzciński, and Patrick Pérez. Clip-dinoiser: Teaching clip a few dino tricks for open-vocabulary semantic segmentation. In *European Conference on Computer Vision*, pages 320–337. Springer, 2024. 1, 2, 5
- [56] Gui-Song Xia, Jingwen Hu, Fan Hu, Baoguang Shi, Xiang Bai, Yanfei Zhong, Liangpei Zhang, and Xiaoqiang Lu. Aid: A benchmark data set for performance evaluation of aerial scene classification. *IEEE Transactions on Geoscience and Remote Sensing*, 55(7):3965–3981, 2017. 4, 3
- [57] Gui-Song Xia, Xiang Bai, Jian Ding, Zhen Zhu, Serge Belongie, Jiebo Luo, Mihai Datcu, Marcello Pelillo, and Liangpei Zhang. Dots: A large-scale dataset for object detection in aerial images. In *Proceedings of the IEEE conference on computer vision and pattern recognition*, pages 3974–3983, 2018. 3
- [58] Junshi Xia, Naoto Yokoya, Bruno Adriano, and Clifford Broni-Bediako. Openearthmap: A benchmark dataset for global high-resolution land cover mapping. In *Proceedings of the IEEE/CVF Winter Conference on Applications of Computer Vision*, pages 6254–6264, 2023. 4
- [59] Rui Xiao, Sanghwan Kim, Mariana-Iuliana Georgescu, Zeynep Akata, and Stephan Alaniz. Flair: Vlm with fine-grained language-informed image representations. In *Proceedings of the Computer Vision and Pattern Recognition Conference*, pages 24884–24894, 2025. 3
- [60] Chunyu Xie, Bin Wang, Fanjing Kong, Jincheng Li, Dawei Liang, Gengshen Zhang, Dawei Leng, and Yuhui Yin. Fg-clip: Fine-grained visual and textual alignment. *arXiv preprint arXiv:2505.05071*, 2025. 2, 3, 4
- [61] Zhitong Xiong, Yi Wang, Weikang Yu, Adam J Stewart, Jie Zhao, Nils Lehmann, Thomas Dujardin, Zhenghang Yuan, Pedram Ghamisi, and Xiao Xiang Zhu. Geolangbind: Unifying earth observation with agglomerative vision-language foundation models. *arXiv preprint arXiv:2503.06312*, 2025. 2, 3
- [62] Hu Xu, Saining Xie, Xiaoqing Ellen Tan, Po-Yao Huang, Russell Howes, Vasu Sharma, Shang-Wen Li, Gargi Ghosh, Luke Zettlemoyer, and Christoph Feichtenhofer. Demystifying clip data. *arXiv preprint arXiv:2309.16671*, 2023. 8
- [63] Yi Yang and Shawn Newsam. Bag-of-visual-words and spatial extensions for land-use classification. In *Proceedings of the 18th SIGSPATIAL international conference on advances in geographic information systems*, pages 270–279, 2010. 4
- [64] Juan Yeo, Soonwoo Cha, Jiwoo Song, Hyunbin Jin, and Taesup Kim. Atas: Any-to-any self-distillation for enhanced open-vocabulary dense prediction. In *Proceedings of the IEEE/CVF International Conference on Computer Vision*, pages 20390–20400, 2025. 1, 2, 3, 5, 6
- [65] Zhiqiang Yuan, Wenkai Zhang, Kun Fu, Xuan Li, Chubo Deng, Hongqi Wang, and Xian Sun. Exploring a fine-grained multiscale method for cross-modal remote sensing image retrieval. *arXiv preprint arXiv:2204.09868*, 2022. 4
- [66] Zhiqiang Yuan, Wenkai Zhang, Chongyang Li, Zhaoying Pan, Yongqiang Mao, Jialiang Chen, Shouke Li, Hongqi Wang, and Xian Sun. Learning to evaluate performance of multi-modal semantic localization. *arXiv preprint arXiv:2209.06515*, 2022. 3
- [67] Beichen Zhang, Pan Zhang, Xiaoyi Dong, Yuhang Zang, and Jiaqi Wang. Long-clip: Unlocking the long-text capability of clip. In *European conference on computer vision*, pages 310–325. Springer, 2024. 2, 3
- [68] Haopeng Zhang and Qin Deng. Deep learning based fossil-fuel power plant monitoring in high resolution remote sensing images: A comparative study. *Remote Sensing*, 11(9): 1117, 2019. 3
- [69] Yuanlin Zhang, Yuan Yuan, Yachuang Feng, and Xiaoqiang Lu. Hierarchical and robust convolutional neural network for very high-resolution remote sensing object detection. *IEEE Transactions on Geoscience and Remote Sensing*, 57(8):5535–5548, 2019. 3
- [70] Zilun Zhang, Tiancheng Zhao, Yulong Guo, and Jianwei Yin. Rs5m and georsclip: A large scale vision-language dataset

- and a large vision-language model for remote sensing. *IEEE Transactions on Geoscience and Remote Sensing*, 2024. 2, 3, 5, 8
- [71] Kecheng Zheng, Yifei Zhang, Wei Wu, Fan Lu, Shuailei Ma, Xin Jin, Wei Chen, and Yujun Shen. Dreamlip: Language-image pre-training with long captions. In *European Conference on Computer Vision*, pages 73–90. Springer, 2024. 3
- [72] Yiwu Zhong, Jianwei Yang, Pengchuan Zhang, Chunyuan Li, Noel Codella, Liunian Harold Li, Luwei Zhou, Xiyang Dai, Lu Yuan, Yin Li, et al. Regionclip: Region-based language-image pretraining. In *Proceedings of the IEEE/CVF conference on computer vision and pattern recognition*, pages 16793–16803, 2022. 1, 2
- [73] Chong Zhou, Chen Change Loy, and Bo Dai. Extract free dense labels from clip. In *European conference on computer vision*, pages 696–712. Springer, 2022. 1, 4, 5
- [74] Weixun Zhou, Shawn Newsam, Congmin Li, and Zhenfeng Shao. Patternnet: A benchmark dataset for performance evaluation of remote sensing image retrieval. *ISPRS journal of photogrammetry and remote sensing*, 145:197–209, 2018. 4
- [75] Jinguo Zhu, Weiyun Wang, Zhe Chen, Zhaoyang Liu, Shenglong Ye, Lixin Gu, Hao Tian, Yuchen Duan, Weijie Su, Jie Shao, et al. Internv13: Exploring advanced training and test-time recipes for open-source multimodal models. *arXiv preprint arXiv:2504.10479*, 2025. 3, 2
- [76] Pengfei Zhu, Longyin Wen, Xiao Bian, Haibin Ling, and Qinghua Hu. Vision meets drones: A challenge. *arXiv preprint arXiv:1804.07437*, 2018. 3

FarSLIP: Discovering Effective CLIP Adaptation for Fine-Grained Remote Sensing Understanding

Supplementary Material

7. Appendix

7.1. Dense Representation

To obtain the dense feature map, we follow recent training-free OVSS methods to extract patch-level features from the ViT-based vision encoder [25, 73]. Specifically, we refer to the approach in [29], making slightly modifies to the last residual attention block. Let the input to the last attention block be denoted by \mathbf{x} , which consists of a class embedding \mathbf{x}_0 and $h \times w$ patch embeddings. The output feature is computed as

$$\mathbf{y} = \text{CustAttn}(\mathbf{x}) \quad (6)$$

where CustAttn represents a customized attention block without residual connection [25, 29]. It can be specifically expressed as follows:

$$\mathbf{q} = \text{Emb}_q(\mathbf{x}), \quad \mathbf{k} = \text{Emb}_k(\mathbf{x}), \quad \mathbf{v} = \text{Emb}_v(\mathbf{x}). \quad (7)$$

$$\mathbf{A}_{tt} = \text{Softmax}\left(\frac{\mathbf{t}\mathbf{t}^\top}{\sqrt{d_h}}\right), \quad t \in \{q, k, v\} \quad (8)$$

$$\mathbf{A} = \mathbf{A}_{qq} + \mathbf{A}_{kk} + \mathbf{A}_{vv} \quad (9)$$

$$\mathbf{y} = \text{Proj}(\mathbf{A}\mathbf{v}) \quad (10)$$

where the final attention matrix is denoted by \mathbf{A} and the output feature by \mathbf{y} . The final dense feature is obtained by discarding the class embedding \mathbf{y}_0 and reshaping the remaining features into an $h \times w$ feature map.

7.2. Open-Vocabulary Semantic Segmentation

For the OVSS implementation, we compute logits by comparing the visual features described in Sec. 7.1 with text queries. The text queries are generated by applying prompt templates to category labels and encoding the resulting descriptions with the text encoder. For comparison methods based on the CLIP architecture, such as CLIP, MetaCLIP, TIPS, and other RS variants, we also use the approach in Sec. 7.1 to obtain the enhanced dense features. For models trained specifically with dense features optimization, such as CLIPSelf, FineCLIP, and COSMOS, we use the dense features extracted by their own methods.

7.3. Comprehensive Evaluation of Dense Feature Representations

7.3.1. Measuring Feature Discriminability

To evaluate the model’s discriminability of visual features across different categories, we randomly sample instances for each category and compute the Davies-Bouldin Index

(DBI), as defined in Eq. (11), which measures the ratio of within-class scatter to between-class separation.

$$\text{DBI} = \frac{1}{K} \sum_{i=1}^K \max_{j \neq i} \left(\frac{S_i + S_j}{M_{ij}} \right) \quad (11)$$

where K is the number of categories, S_i and S_j denote the average intra-class distances of category i and j , respectively, and M_{ij} is the Euclidean distance between the centroids of categories i and j . Features with higher discriminability exhibit lower DBI values.

Specifically, given a semantic segmentation dataset, we randomly select N samples for each target category. We first extract dense features from the images using the image encoder. Then, for each category, instance-level features are obtained by applying average pooling over the pixels within the ground-truth mask. Finally, we compute the DBI across different categories using these instance features. In our experiments, considering that the number of samples per category varies across datasets, we select only categories with more than N samples and set $N = 256$. We compute the DBI on the test sets of the iSAID, LoveDA, OpenEarthMap, Potsdam, and UAVid datasets, and report the mean values.

7.3.2. Measuring the Alignment Between Region and Language

To assess the alignment between regional visual features and text independently, without being affected by visual localization capability, we simplify the task to a zero-shot instance classification task for a given instance feature. Specifically, we use the instance-level visual features extracted as described in Sec. 7.3.1. The corresponding text features are obtained by encoding templates combined with category labels using the text encoder. Finally, we measure region-text alignment via Top-1 accuracy by comparing each regional visual feature with all category text embeddings. The category and sample settings are the same as described in Sec. 7.3.1.

7.3.3. Measuring Semantic Coherence

Semantic coherence has been repeatedly shown to be crucial for dense prediction tasks. To quantitatively assess this property, we formulate it as a binary classification task on pixel pairs, where the goal is to determine whether two pixels belong to the same category. Specifically, we randomly sample pixel pairs from each image and use the semantic segmentation ground truth to assign binary label: 1 if the pixels belong to the same category, 0 otherwise. We

then extract dense visual features and compute the feature similarity for each sampled pixel pair. Finally, mean Average Precision (mAP) is computed over the similarity scores of pixel pairs and their corresponding ground-truth labels, serving as a measure of semantic coherence. In our experiments, we randomly select 300 images per dataset and 500 pixel pairs per image. We report the mean mAP over the test sets of the iSAID, LoveDA, OpenEarthMap, Potsdam, Vaihingen, and UAVid datasets.

7.4. Training Details

We conducted our experiments on 4×NVIDIA A100 (40GB) GPUs. For the three losses used during training, we consistently set the weights of \mathcal{L}_{glo} , \mathcal{L}_{loc} , and \mathcal{L}_{dis} to 1.0, 1.0, and 0.1, respectively, whenever they were applied. The detailed hyperparameter settings for our analysis experiments are shown in Tab. 12, and those for FarSLIP training are provided in Tab. 13.

Table 12. Hyperparameter settings for analysis experiments. RS5M is used for local-global alignment analysis, while MGRS-200k is used for both region-category and local-global alignment analysis.

Setting	RS5M-2.5M	MGRS-200k
Learning rate	1e−6	4e−7
Epochs	1	10
Weight decay	0.1	1
Warmup steps	1000	250
Batch size	40	40
Scheduler	Cosine	Cosine
Optimizer	AdamW	AdamW

Table 13. Hyperparameter settings for FarSLIP training, where stage-1 is trained on the RS5M dataset and stage-2 on the MGRS-200k dataset.

Setting	RS5M	MGRS-200k
Learning rate	1e−6	4e−9
Epochs	1	10
Weight decay	1	1
Warmup steps	1000	250
Batch size	40	40
Scheduler	Cosine	Cosine
Optimizer	AdamW	AdamW

7.5. Details of MGRS-200k

7.5.1. Data Sources

Our MGRS-200k dataset is curated from 16 object detection datasets, sourced from LAE-COD [43], LAE-FOD [43],

and Det-10 [31]. The detailed dataset composition is shown in Tab. 14. Specifically, four datasets from LAE-COD contain automatically generated object annotations using large vision or multimodal models, while the remaining datasets are derived from publicly available object detection benchmarks. For more details, please refer to [31, 43].

7.5.2. Caption Generation

We perform recaptioning using InternVL3 [75] to generate global descriptions of images by incorporating both the image itself and its associated object information. We produce two versions of textual descriptions with different lengths: a short version for the original CLIP [45] (supporting 77 tokens) and a long version for LongCLIP [67] (supporting 248 tokens), aiming to satisfy the demand for long-text inputs in VLFMs. The prompts used to generate the short and long captions are provided in Tab. 17 and Tab. 18, respectively. Some examples from the MGRS-200k are shown in Fig. 4.

7.5.3. Quality Assessment

We randomly selected 200 samples to manually evaluate hallucinations in captions generated by the MLLM. We use a strict evaluation criteria, considering caption that contain any inaccurate or unnatural descriptions as containing hallucinations. Under these criteria, brief captions can achieve 88% accuracy, while long captions achieve 80% accuracy. We found that the captions are generally accurate, with high correctness in describing object categories and scene content. Even when containing hallucinations, they have minimal impact on alignment performance. The most common hallucinations occur in counting, with occasional occurrences in vague spatial descriptions and references to prompt-specific information (*e.g.*, explicitly mentioning the term “bounding box”). We also observed that in most cases, brief captions are sufficient to describe the scene in detail.

7.5.4. Ablation Study

Since our data source includes Det-10 [31], which already provides existing captions, we conduct an ablation study comparing the re-captioned versions with the original captions. Specifically, we fine-tune models on top of CLIP and evaluate zero-shot classification accuracy, as shown in Tab. 15. The results demonstrate significant improvements in model performance, underscoring the critical role of our high-quality text annotations.

7.6. Effects of Caption Length

Previous studies have emphasized the importance of using lengthy and detailed textual descriptions for fine-grained vision-language alignment [1, 10, 60]. To investigate this factor, we compare the effects of global image-caption contrastive learning using short versus long captions from the MGRS-200k dataset. For long-text encoding, we follow the

Table 14. Statistics of the data sources used in our proposed MGRS-200k, including LAE-COD [43] and LAE-FOD [43], as well as Det-10 [31]. The ‘‘Category num’’ for FAIR1M includes 5 super-classes and 37 sub-classes.

Source	Dataset	Image num	Avg. image size	Object num	Category num
LAE-COD	AID [56]	5,286	600×600	34214	1,380
	NWPU-RESISC45 [9]	28,906	256×256	82,343	1,595
	SLM [66]	152	1024×1024	1,081	106
	EMS [43]	2,566	1024×1024	39,013	1,521
LAE-FOD	DOTAv2 [57]	14,059	1024×1024	213,728	18
	FAIR1M [46]	47,325	600×600	328,073	5(37)
	NWPU-VHR-10 [8]	395	1002×638	1,128	10
	Xview [24]	12,318	1024×1024	326,834	53
	Power Plant [68]	581	574×570	891	4
Det-10	AUAIR [49]	32,820	1920×1080	131,977	8
	CARPK [17]	1,448	1280×720	89,774	1
	DIOR [28]	23,463	800×800	192,465	20
	HRRSD [69]	21,761	992×965	57,137	13
	HRSC [32]	1,055	1112×802	2,976	1
	RSOD [33]	936	1059×902	7,385	4
	Visdrone [76]	6,448	1514×992	158,821	10
Total		199,519		1,667,840	3,147

Table 15. Zero-shot classification accuracy comparison of models fine-tuned on CLIP using recaptioned versus original captions

Caption	SkyScript		AID		EuroSAT		MillionAID		NWPU		PatternNet		RSICB		Mean	
	top1	top5	top1	top5	top1	top5	top1	top5	top1	top5	top1	top5	top1	top5	top1	top5
Original	32.86	63.90	59.40	89.90	37.15	77.41	48.17	74.39	54.72	82.66	52.85	79.03	28.39	70.33	44.79	76.80
Recaption	47.88	77.95	70.05	94.75	41.85	85.96	58.99	87.86	65.31	92.92	68.69	90.73	44.38	81.89	56.74	87.44

Table 16. Performance comparison of different text lengths under different loss settings. Only \mathcal{L}_{glo} is affected by text length.

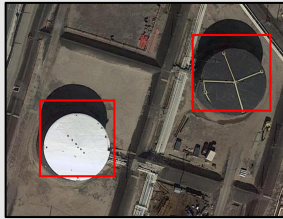
Text length	\mathcal{L}_{glo}	\mathcal{L}_{loc}	ViT-B/16		ViT-B/32	
			ZSC	OVSS	ZSC	OVSS
Short	✓		56.92	35.23	54.04	30.64
	✓	✓	59.17	35.67	58.34	30.56
Long	✓		56.88	35.25	52.38	30.69
	✓	✓	59.24	35.66	58.14	30.44

implementation of Long-CLIP [67]: the original CLIP positional embeddings for the first 20 tokens are preserved, while the embeddings for positions beyond 20 are extended using a 4× interpolation strategy. This extends the maximum supported input length from 77 to 248 tokens.

We evaluate the effect of caption length under two settings: using only \mathcal{L}_{glo} , and using both \mathcal{L}_{glo} and \mathcal{L}_{loc} . Note that caption length only affects \mathcal{L}_{glo} , as it is trained with global-level image-caption contrastive learning. As shown

in Tab. 16, the model trained with long captions shows negligible difference compared to the one trained with short captions. We attribute this to the fact that our short captions are generated via MLLM-based recaptioning, rather than being simplistic web-crawled descriptions. Despite the 77-token limit, these short captions sufficiently capture the rich semantics of RS images in MGRS-200k dataset, as shown in Fig. 4, making the benefits of longer input texts less pronounced.

Nonetheless, we release both the original 77-token-length model and the Long-CLIP variants of our FarSLIP-s2 to accommodate different downstream application needs. In addition, designing methods that specifically leverage long captions for fine-grained alignment [59, 71] could better exploit the potential of the data, which we encourage as a direction for future research.



Short caption: The image shows an aerial view of an industrial area featuring two large aboveground storage tanks. One tank has a white dome, while the other displays a dark surface with a cross-like structure. The tanks are arranged in a rectangular configuration, connected by piping and surrounded by construction and utility equipment, indicating an active industrial site.

Long caption: The image shows an aerial view of an industrial site featuring two large storage tanks. The left storage tank is white, circular, and prominent, situated in a relatively open area. To the right, there's another large, dark circular storage tank with metal supports arranged in a cross pattern on its surface. Nearby, construction materials and equipment are scattered, suggesting ongoing development or maintenance activities. The area is bordered by a network of roads and pathways, enhancing the site's accessibility. This scene captures the typical layout and components found industrial storage facilities.

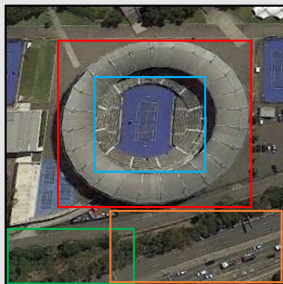
Storage tank



Short caption: The image shows an aerial view of a highway with a large overpass intersecting the road. Two vehicles are traveling on the highway—one on the left side beneath the overpass and another on the right side near the overpass. Surrounding the highway are patches of greenery, open fields, and a small industrial building to the bottom right, providing a contrast of built and natural environments.

Long caption: The image shows an aerial view of a highway infrastructure intersected by an overpass. Beneath the overpass, a pair of vehicles are traveling on the roadway, one on each side. Surrounding the highway are areas of dense greenery, with trees flanking the sides and partially covering sections alongside the road. On the right side, near the bottom of the image, there is a building with a blue roof, adjacent to an open parking area. The roadway is divided into two sections by the overpass, which includes supports embedded within the landscape. The environment combines urban elements such as roads and buildings with natural features like green belts and trees, creating a contrast between developed and undeveloped land.

Overpass Vehicle



Short caption: The image shows a large circular sports stadium with a prominent blue tennis court at its center, surrounded by seating areas. Adjacent to the stadium, there are areas of vegetation and a nearby road bustling with vehicles. The overall layout integrates sport facilities with green spaces and transportation infrastructure.

Long caption: The image presents an aerial view of a sports complex, prominently featuring a large circular sports stadium with an inner court and surrounding seating. Adjacent to and partially visible in the image are several tennis courts, discernible by their rectangular shapes and blue surfaces. The stadium is enveloped by a mix of paved areas and green spaces, with clear demarcations visible through varying textures and colors. At the periphery of the complex, there's dense green vegetation, mainly towards the lower section of the image, contrasting with the more structured, paved roadways that show steady traffic. The road curves around the bottom of the image, suggesting a roundabout or intersection, indicative of the facility's accessibility and integration into the larger urban or suburban infrastructure.

Stadium Tennis court Vegetation Road with vehicles



Short caption: The image captures an aerial view of a sports complex surrounded by vegetation, featuring a large grassy field with adjacent diamond-shaped areas likely used for baseball. Roadways border the complex on multiple sides, and there is a prominent mix of grassy areas and trees, indicating an organized recreational area with open fields for sports. The complex is framed by tree-lined streets and smaller clusters of vegetation, adding to the greenery surrounding the facility.

Long caption: The image displays an aerial view of a sports complex featuring multiple baseball fields and surrounding infrastructure. Dominating the center is a distinctive four-diamond baseball design, with reddish-brown infield bases arranged in a symmetrical cross pattern. Enclosed by a lush green outfield, the complex is flanked by roads and vegetation on two sides, adding a boundary to the recreational area. Nearby, dense clusters of trees, particularly noted in the bottom-right corner, provide a natural backdrop, while streetlights line the adjacent roadways, ensuring the area is well-lit. The spatial arrangement suggests a well-organized and multi-functional play area designed for both sports and recreation, integrated within a verdant neighborhood.

Baseball fields Sports complex Vegetation Roadway Forest

Figure 4. Four examples from our proposed MGRS-200k dataset.

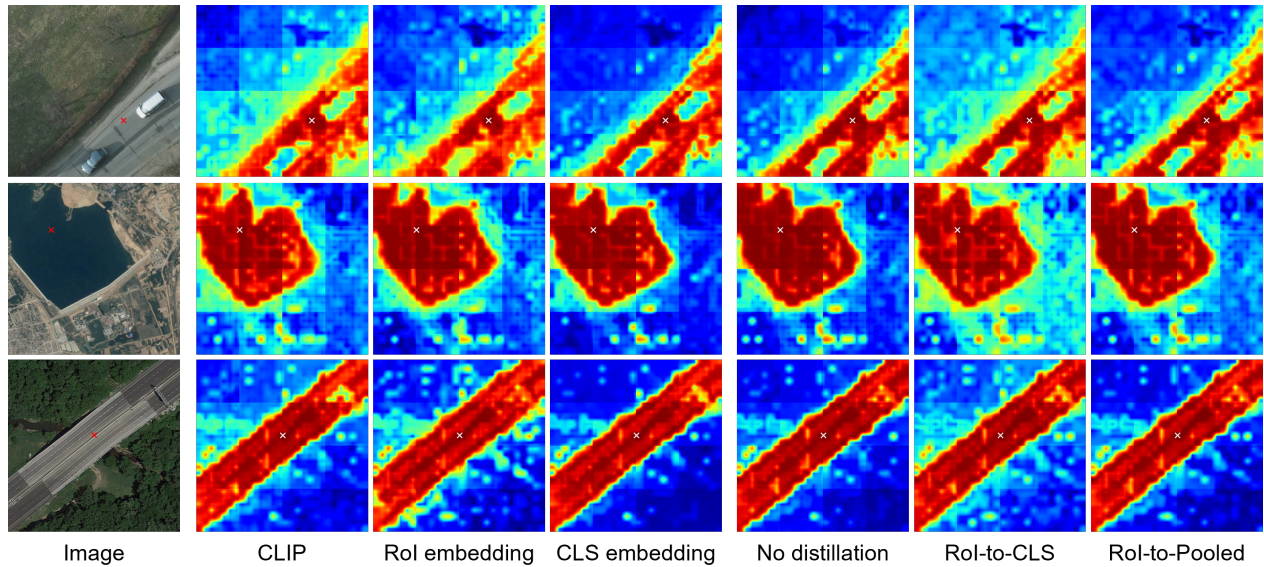


Figure 5. Cosine similarity between the anchor pixel (noted in \times) and all other pixels. Columns 2–4 correspond to the baseline (OpenAI CLIP), ROI embedding-based region-category alignment, and CLS token-based region-category alignment, respectively. ROI-based training tends to disrupt pixel-level semantic coherence, while CLS token-based training enhances it. Columns 5–7 correspond to the baseline (without self-distillation), ROI-to-CLS self-distillation, and ROI-to-Pooled self-distillation, respectively. The CLS token-based approach compromises semantic coherence, whereas ROI-to-Pooled effectively preserves it.

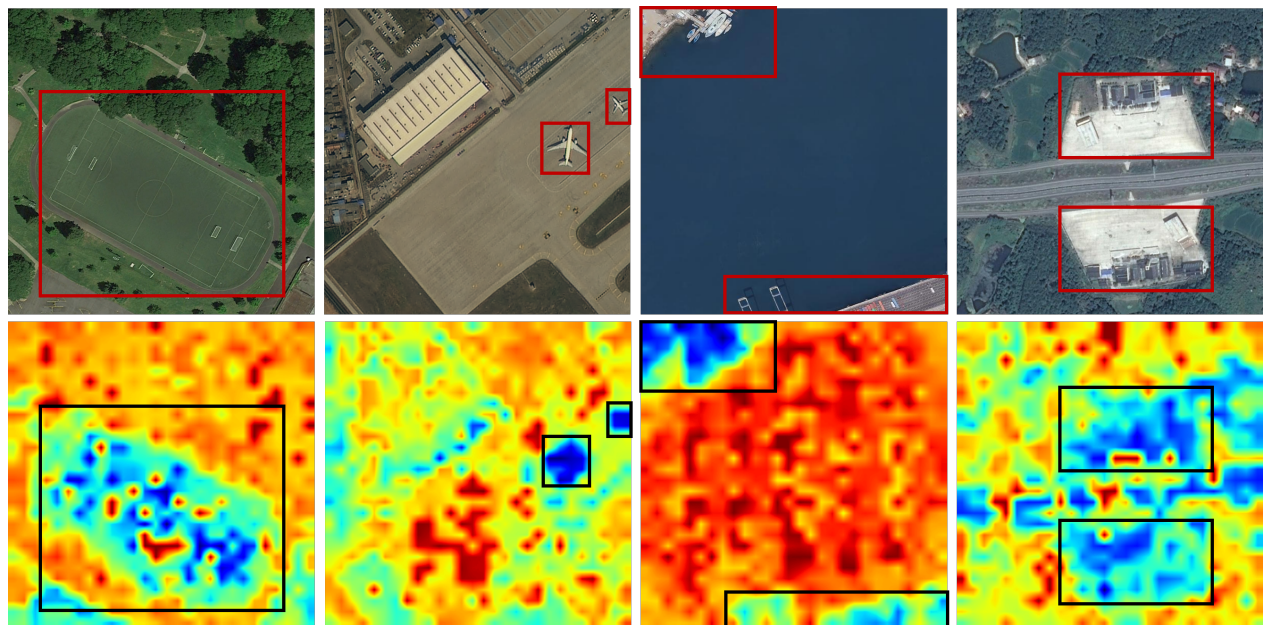


Figure 6. Cosine similarities between the CLS token embedding and all pixels, generated by OpenAI CLIP, show that the CLS token is more similar to the dominant land-cover classes in the image while largely ignoring the relatively minor objects (as indicated by the rectangular annotations). This highlights the risk of losing land-cover recognition in CLS-to-patch self-distillation.

Table 17. Prompt for generating short captions based on RS images and corresponding object information.

You are a remote sensing expert specialized in image interpretation and caption generation. You are provided with a remote sensing image and auxiliary data: a list of object bounding boxes in normalized (x1, y1, x2, y2) format (values between 0 and 1) and their corresponding category labels. Your task is to generate a concise and accurate caption that describes the image content, integrating both visual and object-level information. Follow these principles: (1) Generate a brief caption in two or three sentences that describes the image. (2) Focus on the types of objects present, their spatial distribution, and the relationships between them. (3) Do not include any metadata, annotations, or task instructions in the output — only output a natural-language caption.

{Image}

{Object infos: Category1: Bbox1; Category2: Bbox2, ... }

Table 18. Prompt for generating long captions based on RS images and corresponding object information.

You are a remote sensing expert specialized in image interpretation and caption generation. You are provided with a remote sensing image and auxiliary data: a list of object bounding boxes in normalized (x1, y1, x2, y2) format (values between 0 and 1) and their corresponding category labels. Your task is to generate a detailed, accurate, and fluent caption that describes the image content, integrating both visual and object-level information. Follow these principles: (1) Detailed describe the image starting with a brief summary of the overall scene or environment. (2) If the number of objects is small, describe their attributes, approximate locations, and inter-object relationships. (3) If the number of objects is large, describe the object distribution, density, and spatial patterns. (4) Do not include any metadata, annotations, or task instructions in the output — only output a natural-language caption.

{Image}

{Object infos: Category1: Bbox1; Category2: Bbox2, ... }